Nanoscale

RSC Publishing

PAPER

View Article Online
View Journal | View Issue

Cite this: *Nanoscale*, 2013, **5**, 12365

Optoelectronic properties of graphene thin films deposited by a Langmuir–Blodgett assembly†

HoKwon Kim,*[a] Cecilia Mattevi,*[a] Hyun Jun Kim,[b] Anudha Mittal,[c] K. Andre Mkhoyan,[c] Richard E. Riman[b] and Manish Chhowalla[b]

Received 4th June 2013
Accepted 26th September 2013

DOI: 10.1039/c3nr02907g

www.rsc.org/nanoscale

Large area thin films of few-layered unfunctionalized graphene platelets are developed with fine control over the thickness. The thin films are obtained by a Langmuir–Blodgett assembly at the interface of graphene solution in *N*-methyl-2-pyrrolidone (NMP) and water, and their optoelectronic properties and conduction mechanism are investigated in relation to lateral flake size and thin film thickness. The electrical conductivity and carrier mobility are affected by the flake size (200 nm to 1 μm) and by the packing of the nanostructure platelet network. General effective medium theory is used to explain the thickness dependent conductivity and to determine the percolation threshold film thickness which was found to be about 10 nm (at a volume fraction of ~39%) for a Langmuir–Blodgett film of an average platelet lateral size of 170 ± 40 nm. The electronic behaviour of the material shows more similarities with polycrystalline turbostratic graphite than thin films of reduced graphene oxide, carbon nanotubes, or disordered conducting polymers. While in these systems the conduction mechanism is often dominated by the presence of an energy barrier between conductive and non-conductive regions in the network, in the exfoliated graphene networks the conduction mechanism can be explained by the simple two-band model which is characteristic of polycrystalline graphite.

Introduction

The synthesis and processing in liquid phase of two-dimensional (2D) atomically thin materials, such as graphene[1,2] and metal dichalcogenides,[3,4] have attracted increasing interest in the last few years. The interest is driven by the possibility to scale up the synthesis of these materials making them cheaply available in a large amount enabling a wide range of applications such as large area electronics on transparent flexible/stretchable substrates,[5,6] composites,[7,8] catalytic systems.[9,10] In particular, their integration in the large area of transparent electronic devices necessitates development of colloidal suspensions of 2D platelets and deposition methodologies in order to achieve high quality thin films with controlled thickness over wafer-size areas.

To optimize the film quality and functionality, it is of critical importance to understand the electrical properties of these materials organized in nanostructured networks.[11,12] Similarly, in the last decade, the quality of ultra-thin films of transparent and conductive 1D materials such as nanowires and carbon nanotube have been largely benefiting from rational comprehension of the conductivity from the macro to the nanoscale *via* understanding the charge carrier percolation behavior.[11,13,14]

One of the most promising synthesis routes for liquid phase processed graphene is non-covalent exfoliation of graphite in organic solvents that have compatible surface energy values with that of graphite.[2,15] This method enables the mass production of high crystal quality graphene flakes without chemical modifications. For instance, graphene thin films obtained by ink-jet printing of graphene suspensions in *N*-methyl-2-pyrrolidone (NMP) have shown carrier mobilities up to 95 $cm^2\ V^{-1}\ s^{-1}$,[16] which can extensively enable electronic applications on flexible substrates. Despite the significant attention that pristine graphene platelets dispersed in organic solvent have raised,[17] the reproducible thin film deposition and understanding of the graphene nanostructured network electrical properties are still limited.

Efficient deposition of all monolayers, well distributed flakes has been achieved for solution processed, covalently functionalized graphene with simple vacuum filtration[18,19] and spin-coating[20,21] techniques. In this case, the flakes were deposited mostly as monolayers on large areas, achieving a very low

[a]*CASC, Department of Materials, Imperial College London, Prince Consort Road, London, SW7 2AZ, UK. E-mail: hknano@gmail.com; c.mattevi@imperial.ac.uk; Tel: +44 (0)275940833*

[b]*Department of Materials Science and Engineering, Rutgers University, Piscataway, New Jersey 08854, USA*

[c]*Department of Chemical Engineering & Materials Science, University of Minnesota, 151 Amundson Hall, 421 Washington Avenue SE, Minnesota 55455, USA*

† Electronic supplementary information (ESI) available: Details on the absorbance calculations, additional figures on thin film deposition techniques, thickness *vs.* number of deposition plot, transmittance *vs.* sheet resistance plot with literature data, and temperature dependent hole mobility plot. See DOI: 10.1039/c3nr02907g

percolation threshold.[21] However, the high solubility of the filter material in NMP and the high viscosity and boiling point of NMP hinder the possibility to use vacuum filtration and spin-coating based techniques.

To overcome this challenge, here, we systematically study the optoelectronic properties of graphene thin films obtained by Langmuir–Blodgett (LB) assembly realized at the interface of graphene suspension in NMP and water, as an alternative method to achieve the uniform thin films. Graphene inks in NMP with high concentration ($\sim$1 mg mL^{-1}) and thin films with fine control over the thickness have been obtained using LB deposition. A rational investigation of the conduction mechanism as a function of flakes size and film thickness has been carried out in order to uncover the electrical conduction mechanism in the framework of the percolation theory as well as in the light of charge carrier transport models.

Experimental procedure

Preparation of graphene in NMP

Graphite and NMP were obtained from Sigma-Aldrich. Before mixing, large particles of graphite were removed by a 125 μm mesh sieve. The mixture with an initial graphite concentration of $\sim$200 mg mL^{-1} was then sonicated in ultrasonic bath while being stirred by a custom made stirrer. For each experiment, great care was taken to maintain the level of water and position of the beaker containing the mixture in the ultrasonic bath to ensure reproducibility. The mixture was then purified by centrifugation (Beckman Coulter Avanti J-26 with JA-20 rotor), with centrifugal force of 12 000 rpm (r.c.f. = 10 000 g) for 30 min. We note that the centrifugation step must be followed right after the sonication/stirring step with minimal delay between the steps to prevent re-aggregation. The top 80% of the supernatant was taken out from the centrifuge tube and stored in vial for further experiments. Refer to Scheme 1 for the overall illustration of the procedure. For thin film deposition, three main types of dispersions (GNMP1, GNMP2, and GNMP3) were produced by varying the sonication time only (20, 30, and 60 min) while the other parameters were fixed as noted above.

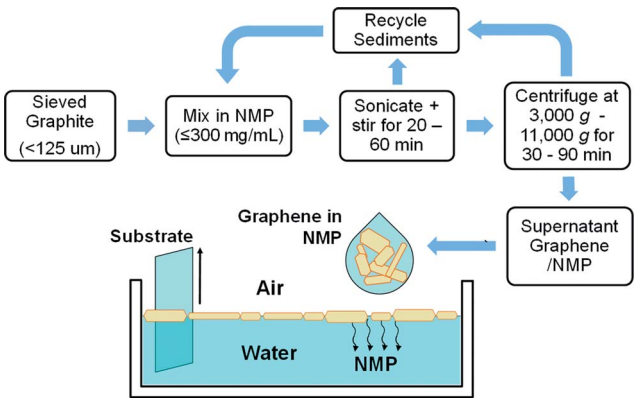

Scheme 1 Graphene exfoliation in NMP and Langmuir–Blodgett deposition process. The exfoliation step is largely adapted from the work by Y. Hernandez *et al.*[2] In order to significantly improve the efficiency and yield, we have introduced simultaneous stirring during the sonication step.

Thin film deposition

For the facile, large scale deposition (*e.g.* on glass slides for transmission measurements), we utilized an automated dip-coater system to control the speed of the substrate's vertical movement [Fig. S1b in ESI†], and an automatic syringe pump to simultaneously control the input rate of graphene dispersion dropped onto the surface of water in a modified Langmuir–Blodgett deposition scheme known as fluid forming (Fig. S2 in ESI†).[22,23] Here, the floating layer of graphene on water is kept uniform by the continuously dropping the dispersion from the syringe onto the water surface to provide enough surface pressure for the film to be close-packed while the layer, with the substrate, is being pulled out from the bath. For deposition on small scale SiO_2/Si substrates for FET device measurements, we have employed a simpler, Langmuir–Schaefer deposition method[24] (Fig. S1c in ESI†) where the substrate was pulled from the water bath horizontally after the formation of a complete layer.

Concentration measurement

To estimate the concentration of dispersed graphene in NMP, optical absorbance measurement on the dispersions was performed using a UV-vis spectrophotometer (S2000-UV-ViS, Ocean Optics, Inc.). Concentration was calculated from Beer–Lambert's Law using the absorptivity of graphene dispersion placed in quartz cuvette at 660 nm, $\langle\alpha_{660}\rangle = 3600$ L g^{-1} m.[25,26]

Raman spectroscopy

Raman Spectroscopy was carried out in a Reinshaw InVia Raman spectrometer at the excitation wavelength of 632 nm from He–Ne laser using 100× objective lens (spot size <2 μm).

Atomic force microscopy

The morphology and thickness of the graphene thin films were investigated by Veeco NanoScope Multimode AFM. Tips used were AFM Si Tip NSC15 (tip radius, 10 nm) for tapping mode AFM.

Van der pauw sheet resistance measurement

4-Probe van der Pauw measurement was performed on our thin films deposited on glass or SiO_2/Si(100) substrates using a probe station equipped with four tungsten probes connected to Keithly 2400 SourceMeter.

Two probe and field effect measurement

FET structure was fabricated by depositing the graphene film on thermally grown 300 nm SiO_2 on heavily p-doped Si(100) substrate as back gate and depositing >30 nm thick patterned Au electrodes with channel length of 20 μm and width of 500 μm by thermal evaporation through a shadow mask. The source to drain current was measured as a function of applied gate voltage in a probe station equipped with pre-programmed parametric analyzer (hp4140B). The temperature dependent

conductivity and field effect measurements were performed in a cryostat (ST- 500, Janis) at temperatures ranging from 78 K (liquid nitrogen was used as the coolant) to 300 K in a high vacuum (10^{-5} torr base pressure).

Optical transmittance measurement

The transmittance of Langmuir–Blodgett graphene films was obtained in the visible range of electromagnetic spectrum using a UV-visible spectrophotometer (S2000-UV-ViS, Ocean Optics, Inc.).

Results and discussion

Graphene dispersion in NMP

The initial conditions of exfoliation of graphite in NMP used in this study were based on the method developed by Y. Hernandez *et al.*[2] as displayed in Scheme 1. The effect of the exfoliation conditions such as the initial concentration of graphite powder, sonication time (t_s), centrifugation speed/time, and additional stirring process has been investigated further in order to optimize the method to yield high quality, well-exfoliated graphene dispersions of high concentrations. Fig. 1 shows the photographs of graphene dispersions prepared using various exfoliation conditions.

High rotational speed of centrifugation generally reduces the amount of unexfoliated graphite in NMP, however it also significantly decreases the concentration of the final supernatant as can be seen in Fig. 1. Applying stirring to the mixture (Scheme 1) during the sonication step has been found to markedly improve the concentration of the exfoliated graphene by more than an order of magnitude (Fig. 1d and e). The absorbance measurement of the dispersion has shown that graphene concentration of ~1 mg mL^{-1} can be obtained by simultaneously stirring and sonicating the mixture of initial graphite concentration of 200 mg mL^{-1} for 30 min followed by centrifugation at 12 000 rpm.

The significant improvement in the concentration can be explained by shear thinning.[27–29] When the initial concentration of graphite is more than 500 mg mL^{-1}, the suspension becomes viscous in a gel-like state that would dramatically damp out the ultrasonic excitations. Rotation of the stirring shaft induces shear in the mixture to momentarily increase the fluidity and allow the sonication to remain effective so that final concentration of >1 mg mL^{-1} can be obtained within tens of minutes of sonication time. This increased efficiency is a significant improvement over previous report by Khan *et al.*[30] where sonication time of more than two weeks would be required to achieve the similar concentration of graphene without the application of stirring. Higher concentration of ~27 mg mL^{-1} was recently demonstrated although it required an extra step of redispersing vacuum filtered exfoliated graphene films in NMP.[25] It should be also noted that attempt to increase the concentration by drying the dispersion on a hotplate in air leads to oxidation and oligomerization of NMP,[31,32] thus degrading the quality of dispersion and leaving behind solid residues after the evaporation of the solvent.

Characterization of exfoliated graphene

Thickness, crystal quality, and lateral sizes of the flakes obtained in the purified supernatant were characterized after the centrifugation of the exfoliated graphene dispersions. The Raman spectroscopy on the drop-cast and Langmuir–Blodgett films was used to determine the thickness of individual graphene flakes by analyzing the shape and position of the 2D peak of the spectra (Fig. 2). Comparison with the 2D peaks reported in the literature for mechanically exfoliated graphene indicates that most of the individual graphene flakes have thickness of 2–5 layers (in excess of 90%) reflecting that the flakes have been well exfoliated.[33]

To investigate the crystal quality of graphene, the D to G peak intensities ratios and G peak FWHM have been analyzed for the same Raman spectra. As evident in Fig. 2, the G to D peak intensity ratio (1.3–1.4) of NMP exfoliated graphene is much less than that of graphene oxide and closer to that of the starting graphite.[34] Furthermore, the FWHM of the G peak remains unchanged indicating good crystallinity. The presence of the D′ peak can be correlated with presence of various type of defects as observed in defective graphene.[35] As expected for the non-covalent exfoliation, the degree of defect appears to be much less than that of covalently functionalized graphene.[18,34] The main reason for the appearance of the significant D and D′ peaks following exfoliation from the starting graphite is likely due to

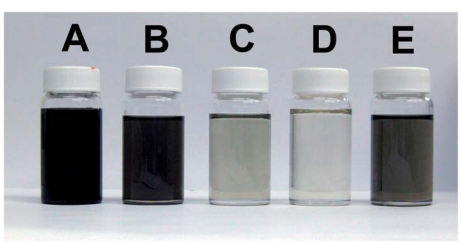

Fig. 1 Effect of centrifugation speed and stirring on the solute concentration. Photographs of (A): supernatant solution before the final centrifugation step, (B): supernatant after centrifugation at 3000 rpm for 30 min without stirring, (C): supernatant centrifuged at 6000 rpm for 30 min without stirring, (D): supernatant centrifuged at 12 000 rpm for 30 min without stirring, and (E): supernatant centrifuged at 12000 rpm for 30 min with stirring applied.

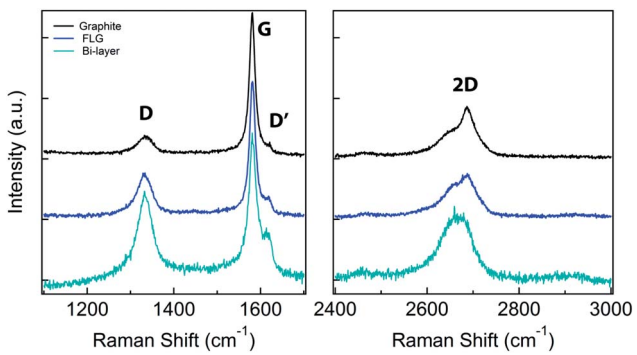

Fig. 2 Raman spectra of graphite, exfoliated few layer graphene (FLG), and exfoliated bilayer graphene deposited on SiO_2/Si substrate from the graphene/NMP suspension. Laser excitation wavelength: 633 nm.

the edge defects of exfoliated graphene flakes of smaller lateral sizes (<200 nm) that are produced during the vigorous exfoliation process.[36] Thus, the lower number of layers in the graphene flakes often results in higher D and D′ peak intensities as the thinner, well exfoliated graphene flakes are likely smaller in lateral size exhibiting higher density of edge atoms per unit area.

Fig. 3 shows the C 1s signal of fully exfoliated graphene in NMP of five different chemically shifted components which can be deconvoluted into: C=C/C–C in aromatic rings (284.5 eV); C–O and C–C sp^3 (285.8 eV); C=O (287.5 eV); C(O)–(OH) (289.1 eV); and π–π* satellite peak (290.7 eV). These assignments are in agreement with previous works.[37,38] We fit the C 1s peak component related to sp^2 C=C/C–C bonding with Doniach–Sunjic line shape with zero asymmetry due to the absence of C–C sp^3 (binding energies in range 285.5–286.5 eV[38]) bonding which has been accounted separately. The oxygen signal detected is likely due to the residual of NMP and oxygen functionalized edges on graphene.[2]

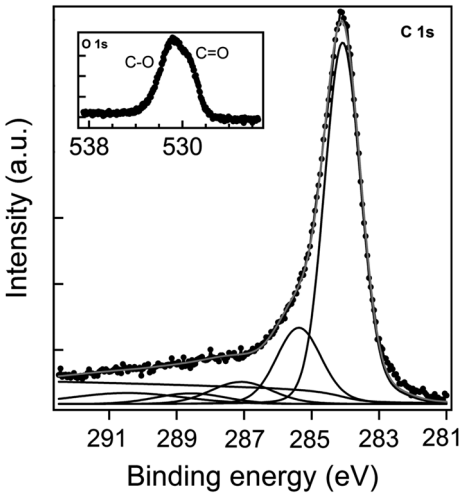

Fig. 3 C 1s XPS spectra (E_{hv} = 1253.6 eV) collected on GNMP2 thin film deposited on Au (100 nm) – SiO_2 (300 nm) – Si substrate. The fitting was performed on the spectra after background subtraction by a Shirley background.

Further support for the in-plane crystallinity of the graphene flakes was provided by high resolution TEM (images shown in Fig. S3 in SI†) where lattice fringes can be clearly seen from the exfoliated flakes, indicating a good crystal quality within an individual flake.

Properties of Langmuir–Blodgett deposited films

The LB deposited films deposited on glass and Si(100) substrates with 300 nm thick thermally grown SiO_2 were dried in at 420 °C in forming gas [Ar (90%) and H_2 (10%)] for 30 min in order to truly remove any residual solvents. Representative AFM scans of LB films obtained from dispersions of graphene prepared using the three different sonication times (t_s = 20 min, GNMP1; t_s = 30 min, GNMP2; t_s = 60 min, GNMP3) are shown in Fig. 4a–e. It is possible to observe that the lateral size of the graphene flakes decreases as the t_s increases as shown in the flake size distribution (Fig. 4f). This is consistent with general sonication phenomena of particle scission where the dimensions of particle decrease as $t_s^{-1/2}$.[25,36,39,40] The SEM images of the LB films are provided in ESI (Fig. S4†).

A problem often seen in the case of drop-cast or vacuum-filtered film of graphene/NMP is that poor wetting and slow drying time of the solvent induce aggregation of exfoliated graphene flakes hindering a fine control over the film thickness.[2,41] Langmuir–Blodgett deposition allows reliable and reproducible thickness control and prevents further agglomeration of the graphene fakes during drying. However, an individual deposition results in thicker than 4–5 layered graphene film overall, and not in a mono-atomically thin film as it occurs for graphene oxide LB assembly. This is due to the lack of strong repulsive forces between flakes as occurs for graphene oxide, which can be dispersed completely as monolayer flakes, with consequent easy flakes flocculation occurring in particular when in contact to the water interface.[42,43] Flocculation is further driven by repulsion between the hydrophobic graphene platelets and water interface, subsequent minimization of water–graphene interfacial area contact leads to the overlap of the graphene flakes while lower surface energy of graphene in

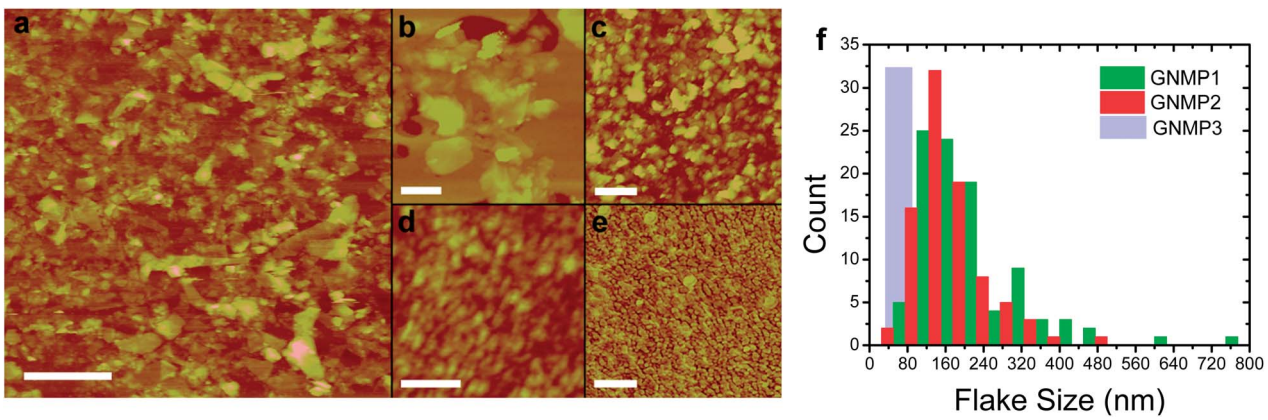

Fig. 4 Atomic force microscopy height image LB films of different types of graphene in NMP and different number of deposition, *n*. (a) GNMP1, $n = 1$ (scale bar: 800 nm), (b) GNMP2, $n = 2$ (scale bar: 200 nm) (c) GNMP2, $n = 5$ (scale bar: 1 μm), and (d) GNMP3, $n = 2$ (scale bar: 200 nm). (e) AFM Phase image of GNMP3 with $n = 2$ (Scale bar: 400 nm). (f) Lateral size distribution of graphene flakes obtained from the AFM images of LB films for the three different types of suspensions.

contrast to the surface energy of water prevents further aggregation. Similar flocculation/separation behavior has been observed when water was added to an oil-NMP interface.[44] The effect of the overlap between the flakes is apparent in the lateral flake size dependent LB film thickness where the dispersion with larger average flake size results in higher thickness per deposition [Fig. S5 in ESI†] Lower thickness can also be achieved by decreasing the concentration of graphene suspension in NMP, however with consequent increase of pinholes in the graphene films and increased inhomogeneous flakes distribution. The average thickness for each deposition (~7 nm for GNMP2) was nevertheless consistent as it appears to increase linearly with the number of deposition [Fig. S5 in ESI†]. It must be noted that GNMP2 was mainly used for the thickness dependent measurement as it allowed the balance between the yield and lateral size of the flake.

Optoelectronic characteristics of Langmuir–Blodgett films

The optical transmittance of the LB film in the visible spectrum displays consistent decrease in transparency with increasing film thickness (Fig. 5). The highest transparency (considered at $\lambda = 550$ nm) for a single deposition (produced from GNMP3), was found to be about 98%, which is higher than the transmittance that we would expect for ~7 layer film. This is due to the loose stacking of graphene sheets and presence of empty spaces between flakes that result in a large density of pinholes. Increasing the graphene film thickness led to a consistent decrease in transparency, however, down to 55% for 5 layers. From the thickness *versus* transmittance behavior of GNMP2, the calculated absorption coefficient is 0.0076 nm^{-1} (at $\lambda = 550$ nm) which is indeed much less than that of an ideal graphene film (0.03 nm^{-1})[45,46] as expected from the loosely packed structure (Fig. 4; details on the curve fitting and absorption coefficient calculations are included in ESI†).

Electrical characterization has shown that the conductivity of a thin film of approximately 7 nm of thickness significantly increases after annealing by at least three orders of magnitude, confirming the importance to minimize the NMP residuals.[2] The electrical conductivity is also affected by the size of the flakes as well as the thickness of the films. The film with the largest average flake sizes, 220 nm (Fig. 6a), exhibited the highest conductivity of 100 S cm^{-1} (GNMP1) while the film with the lowest average flake size of 80 nm (GNMP3) exhibited much lower conductivity of 0.0044 S cm^{-1}. This dependence of the conductivity on the flake sizes suggests that the sheet-to-sheet junction resistance affects the charge transport as previously reported for the ultralarge graphene oxide LB thin films.[47] However, the conductivity also increases with thickness of the films (Fig. 6a), suggesting that the presence of pin-holes are responsible for the reduced electrical properties of the thin films.[48] The thickness dependent behavior can be further understood in the framework of percolation theory.

The difference between the bulk film and thin film of exfoliated graphene can be attributed to reduced effective volume fraction due to the volume that does not participate in charge carrier conduction at the surface.[41] We assign a thickness to this

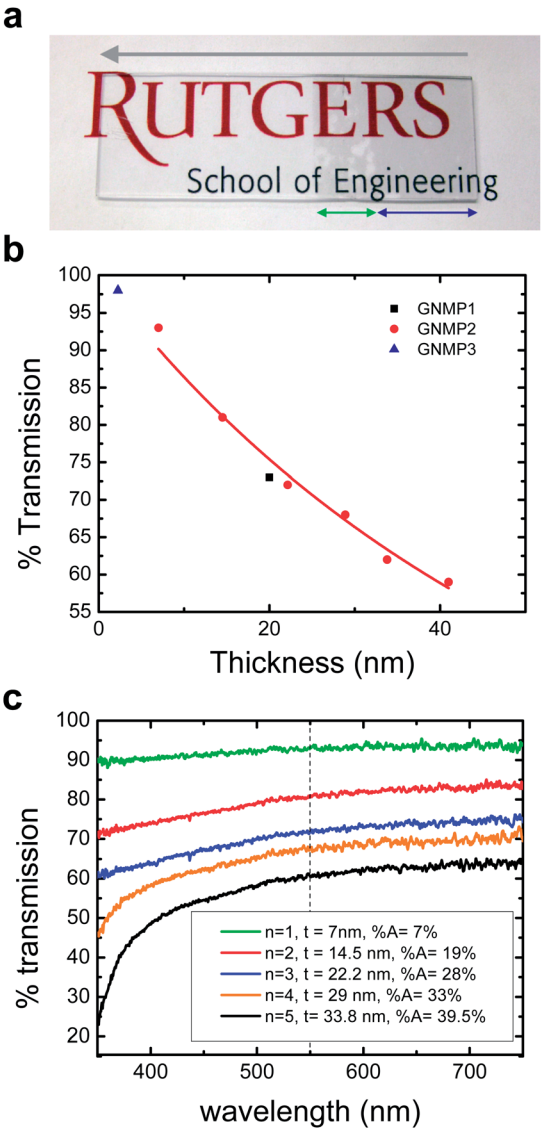

Fig. 5 (a) GNMP2 deposited onto a glass slide by the Langmuir–Blodgett deposition method. Grey arrow line indicates the direction of vertical movement of substrate during the LB deposition. Green line region indicates initial stage of deposition where the film contains pin-holes and non-uniformity. Blue line region indicates homogenous film deposition after the initial stage. (b) %transmittance (at 550 nm) *versus* thickness plot of LB thin films deposited on glass slides from the three types of dispersions, GNMP1, GNMP2, and GNMP3. The curve fit was performed for GNMP2 for the absorption coefficient calculations (Details given in SI). (c) Optical transmittance for different number of LB deposition, *n*, on glass in the visible spectrum (from GNMP2). Percent absorption (%A) at 550 nm for each thickness is indicated in the legend.

non-percolative volume, Δt, and approximate the effective volume fraction to be $\phi = t/(t + \Delta t)$. Using a simplified form of generalized effective medium (GEM) model of percolation, the relationship for the thickness conductivity, $\sigma_{dc}(t)$ above the critical percolation thickness, t_c can be written as:[49,50]

$$\sigma_{dc}(t) = \sigma_{bulk}^{DC}\left(\frac{t - t_c}{t + t_c}\right)^p \quad (1)$$

here, we assume $t_c = \Delta t$ which is a threshold thickness for formation of percolative network of graphene flakes. p is a

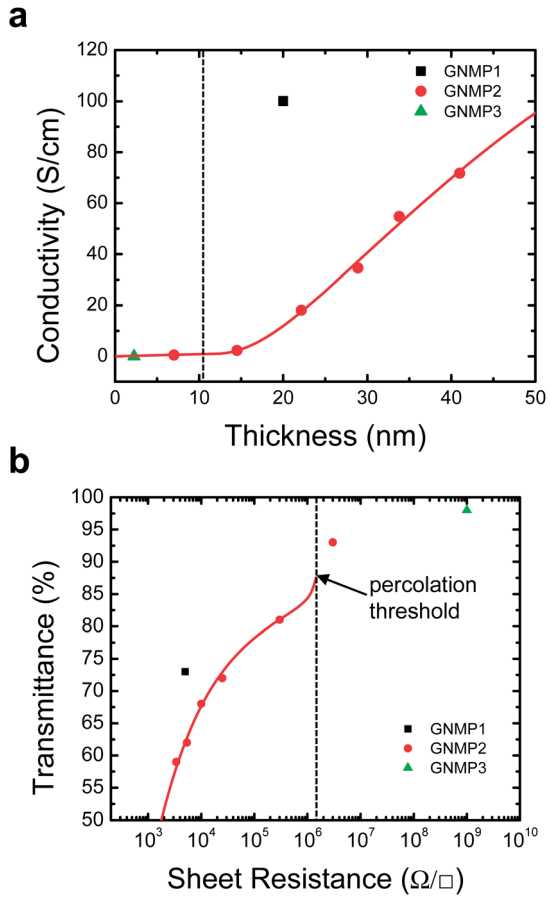

Fig. 6 (a) Conductivity *vs.* thickness graph for LB films. The curve fitting was performed on GNMP 2 data sets according to eqn (1) for $t > t_c$. Linear extrapolation was used for $t < t_c$. (b) Transmittance *vs.* sheet resistance graph for LB Films for different number of deposition. The curve fitting was performed according to eqn (2). The dashed line indicates the percolation threshold for GNMP2.

critical percolation exponent related to the geometry and interaction between the flakes,[49,50] and σ_{bulk}^{DC} is the bulk conductivity as t approaches infinity. The curve fitting performed on the conductivity *versus* thickness for GNMP2 shown in Fig. 6a predicts the threshold thickness t_c to be ~11 nm or critical volume fraction, ϕ_c of ~39%. This value is in a reasonable agreement with the increase in the conductivity displayed after the second deposition. Indeed, we expect the first layer (t = 7 nm) to be just below t_c because of the non-uniform coverage with pinholes and most of the contacts between the graphene flakes are made through only their edges.[42] After the 2nd deposition (t > 14 nm), the overlap between the graphene flakes should be large enough for the percolation to take place.

One can also employ the average interparticle distance (IPD) model[51–53] to predict the percolation threshold of the film considering the individual flakes as circular disks that:

$$\phi_c = \beta \frac{D^2 t_{disc}}{(D + D_{IP})^3} \quad (2)$$

where D is the average diameter or lateral flake size, t_{disc} is the thickness of the exfoliated flake, D_{IP}, average inter-particle hopping distance (D_{IP} < 10 nm), and β is a geometric factor that depends on the orientation and size distribution of the flakes. For example, $\beta = 27\pi/4$ for randomly oriented discs of uniform diameter of D, and $\beta = \pi/4$ for horizontal aligned parallel discs of uniform diameter. Taking the average lateral size of GNMP2 ($D \sim 170$ nm) and $t_{disc} \sim 1$ nm, β for our experimental system is calculated to be 66, even larger than the randomly oriented case ($27\pi/4 \cong 21.2$).

This deviation, resulting in a percolation threshold value that is larger than expected is likely due to the roughness of the film, folding aggregation of the flakes, and large size and shape variations, as reported previously for graphene nanosheet based composite in $Li_4Ti_5O_{12}$ matrix.[53]

The obtained value of the percolation exponent, $p = \sim 2.5$ is moderately greater than what is predicted by scaling arguments for isotropic systems ($p = \sim 2$ for 3D systems;[54] $p = \sim 1.3$ for 2D[55]). However, the high values of the exponents ($p > 2$) were also experimentally found in the other similar thin film systems of exfoliated graphite[11,16,56] and can be attributed to the highly anisotropic dimensions and orientation of the graphene flakes.[49] Similar percolation behavior is expected for other films (GNMP1 and GNMP3) although with different values of t_c and p.

From the fitting, we can see that the $\sigma_{DC}(t)$ values in the range of thickness of practical importance (T > 50%) is well below the bulk graphite DC conductivity, and $\sigma_{DC}(t)$ is only attained when $t \gg 100$ nm. Further insights regarding the optoelectronic properties of the films in the light of the percolation framework can be obtained by calculating the DC conductivity to optical conductivity ratio for different film thicknesses, as this is the figure of merit for any transparent conductors. To do so, consider the relationship between optical transmittance and sheet resistance, R_s for thin films:[41]

$$T = \left(1 + \frac{Z_0}{2R_s}\frac{\sigma_{Op}}{\sigma_{DC}(t)}\right)^{-2} \quad (3)$$

where $Z_0 = 376.7\ \Omega$, is the impedance of free space and σ_{Op} is the optical conductivity of the film which is constant in the thickness ranges investigated. Using this equation, we can fit the T *versus* R_s data in Fig. 6b and to extract σ_{Op} based on the calculated values of $\sigma_{DC}(t)$ from Fig. 6a. Interestingly, the fitted curve well depicts the thickness dependent behavior of R_s *versus* the optical transmission above the percolation threshold where t > 7 nm. Considering the effect of percolation, the film with the largest mean flake size (GNMP1) exhibited the lowest sheet resistance R_s of 5 kΩ/□$^{-1}$ at transmittance of 73% (Fig. 6b) and $\sigma_{DC}(t)/\sigma_{Op}$ ratio of 0.48 (at thickness of 20 nm). This is comparable to other similar solution processed graphene films reported in literature[2,16,30,48,57–63] (Fig. S6 in ESI†), however, $\sigma_{DC}(t)/\sigma_{Op}$ values can be further increased by careful optimization of the deposition conditions (*e.g.* reduction of pinholes by applying lateral surface pressure during the LB deposition) to improve the percolation parameters so that σ_{DC}^{bulk} can be reached at lower thickness. σ_{DC}^{bulk} obtained for GNMP2 from the curve fitting in Fig. 6a is about 300 S cm^{-1} which is still lower than that of bulk graphite (>10 000 S cm^{-1})[64] and σ_{DC}/σ_{Op} ratio of 11.[65] From the optical density of our film obtained by comparing the value of absorption coefficient with that of ideal multilayer graphene,[45,46] we estimate that the maximum

possible conductivity of fully densely packed film would be ~1200 S cm^{-1} which is on the same order of magnitude of polycrystalline pyrolytic graphite.[64]

Field effect has been observed in our thin film field effect transistor (FET) devices built on SiO_2(300 nm)/Si wafer. The transfer characteristics of the FET devices shown in Fig. 7a indicate that the on/off ratio is between 1 and 2, even for a large voltage sweep (from −100 V to 100 V). In addition, the film was found to be heavily p-doped with the charge neutrality point located at a gate voltage (V_{GS}) greater than 40 V. This is possibly due to the residual solvents trapped between the sheets and doping from the edge states and defects which act as electron traps[64] and from the doping induced by the hydroxyl groups at the SiO_2 surface. We also observed the hysteresis effects for different sweeping directions and saturation currents at high bias voltages, confirming the role played by the substrate.

From the slope of the transfer characteristics, the field effect carrier mobility (μ_{FET}) values can be calculated by eqn (3):[66]

$$\mu_{FET} = \frac{I_{ds}}{C_{ox}\frac{W}{L}V_{DS}V_{GS}} \quad (4)$$

where C_{ox} is the oxide capacitance ($C_{ox} = \varepsilon_{ox}\varepsilon_0/t_{ox}$), W, the channel width, L, the channel length, and V_{DS} the source to drain voltage. The hole mobility at room temperature value were around 0.9 $cm^2\ V^{-1}\ s^{-1}$ while the average electron mobility was about an order of magnitude smaller than the hole mobility. It is worth noting that the measured value of μ_{FET} is an underestimate of the actual carrier mobility as percolated conductive paths comprise only a fraction of the film area. Mobilities of up to ~95 $cm^2\ V^{-1}\ s^{-1}$ was recently observed in sprayed coated films of graphene exfoliated in NMP.[16] However, this was achieved only after careful optimization of deposition parameters such as substrate surface functionalization, avoiding the use of bare SiO_2, and packing of graphene flakes.[16]

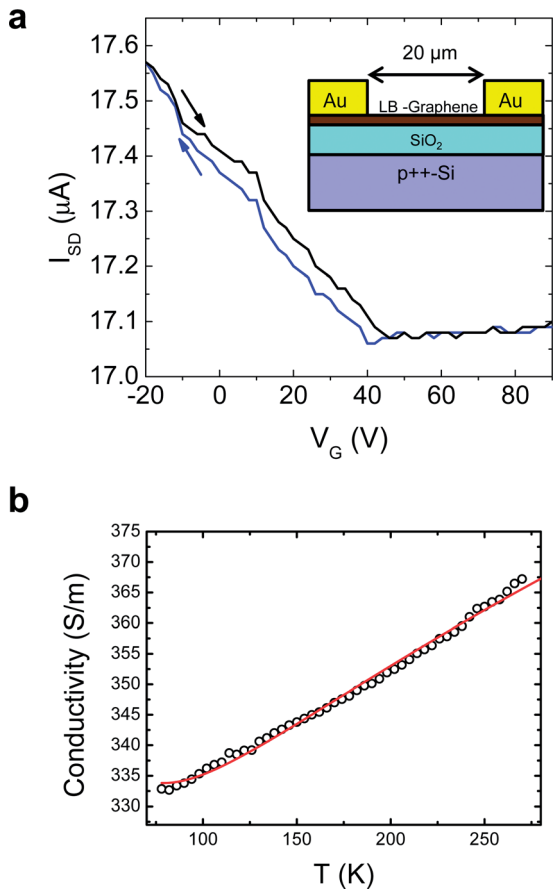

Fig. 7 (a) FET transfer characteristics for GNMP2 thin film ($n = 2$). The arrows on the curves show the direction of gate voltage (V_g) sweep. (b) Temperature dependent conductivity from a GNMP2 device. Curve fit was performed according to the STB model of polycrystalline graphite (eqn (4) and (5)).

Temperature dependent measurements

In order to gain further insights on the limiting factors to the nanoscale electrical properties, we have performed temperature dependent conductivity and mobility measurements in the temperature range between 78 K and 280 K. This will specifically help us to elucidate the transport mechanism of the bulk conductivities (σ_{DC}^{bulk}) as the percolation parameters (p and t_c) can be considered to be independent of temperature. The weak temperature dependence and semimetallic/semiconducting behavior for a GNMP2 device are shown in Fig. 7b. Similar temperature-dependent behavior was observed by P. Blake *et al.* for spray-coated thin films of graphene exfoliated in DMF.[62] The increase in conductivity with increasing temperature has been typically ascribed to various charge localization models such as Mott type variable range hopping (VRH),[67] fluctuation induced tunneling (FIT),[68] and thermal activation conduction,[69] in the case of disordered conducting polymers,[68,70–72] covalently modified graphene,[12,73] and thin film network of carbon nanotubes[74–78] stemming from the presence of energy barrier between conductive regions in the network. However, the weak and almost linear dependence of conductivity with temperature did not yield reasonable values for above models even if the combination of the models were used for different temperature ranges. Our temperature dependent hole mobility behavior also do not support presence of mobility gap in the film at low temperature as the mobility value decreases as the temperature rises (Fig. S7 in ESI†).

Unlike a network of carbon nanotubes that partly contains semiconducting nanotubes and a film of disordered conductors, interaction between the conductive regions of the graphene flakes without strong localization above the percolation threshold is apparent here. This is further supported by the room temperature value of the σ_{DC}^{bulk} approaching that of polycrystalline graphite (Fig. 6a). We can therefore consider the film to be an oriented, polycrystalline mixture of turbostratic graphene and Bernal stacked few-layer graphene, and apply the band theory of charge carrier transport to the temperature dependence carrier mobilities. In a single crystal graphite, a finite overlap between conduction and valence bands leads to a finite density of states at the Fermi level and results in metallic like conduction. However, in pyrolytic graphite of small crystalline size and very thin layer of graphite, the density of the states at the Fermi level diminishes as the overlap becomes very small.[79,80] The conduction behavior, here observed, can be

explained by the simple two band (STB) model of polycrystalline graphite[81–83] where two symmetric parabolic bands are used to describe the density of electrons and holes in conduction and valence bands, respectively. In the case of the heavily p-doped film ($n = n_h \gg n_e$),

$$n(T) = \frac{16\pi}{h^2 c_o} kT \ln\left[1 + \exp\left(\frac{\Delta}{kT}\right)\right] \quad (5)$$

where h is Planck's constant, $c_o = 6.71 \times 10^{-10}$ m, c-axis lattice parameter of graphite, k, Boltzmann's constant, Δ is magnitude of energy level shift in E_F from the charge neutrality point.

The carrier mobility, μ can be described in terms of lattice scattering due to electron–phonon interaction, and boundary scattering.

$$\frac{1}{\mu(T)} = \frac{1}{\mu_b} + \frac{1}{\mu_{th}(T)} = \frac{1}{\mu_b} + BT^{\alpha} \quad (6)$$

where B and α are temperature independent constants.

Therefore, using the Drude formula for conductivity ($\sigma(T) = en(T)\mu(T)$), the conductivity can be fitted according to the STB model as illustrated in Fig. 7b. The curve fitting yielded $\Delta = 2$ meV, which is quite reasonable considering the hole of doping on the order of 10^{18} cm^{-3} as estimated from the position of the charge neutrality point in Fig. 7a. In addition, $\alpha = 0.82$, which is also a reasonable value as it can range from 0.5 to 1.6 in polycrystalline graphite.[84] The deviations from STB theory become apparent at low and high temperature limits, and they can possibly arise from the temperature dependence of contact resistance at the electrode–graphene junction, activation of trapped charges at higher temperatures, inhomogeneous charge carrier density, and temperature dependent α.

The gradual decrease of μ_{FET} with the temperature can also be explained considering that μ_{FET} remains fixed at low temperature as the mean free path is mainly limited by the crystalline size, and at high temperature, mobility is predominantly limited by the thermal scattering of the charge carriers, although the scatter in data points is too large to perform reliable fitting (Fig. S7 in ESI†).

Conclusions

Summarizing, scalable methods for efficient production of highly concentrated solution of high quality graphene in NMP (~1 mg mL^{-1}) and large area deposition of graphene films with variable have been developed. LB deposition have been optimized in order to obtained fine control over the thickness of the films, enabling deposition thickness ranging from 2 nm to 30 nm. The optoelectronic properties have been analyzed in the light of percolation theory and charge transport models. The conductivity of the thin films can be improved by an order of magnitude by increasing the lateral size and denser packing of graphene flakes in the LB assembly and subsequent deposition. Unlike reduced graphene oxide, CNT, and disordered conducting polymer networks, where the conduction mechanism is often dominated by the presence of energy barrier between conductive regions in the network, the temperature dependent conductivity measurement has shown that here the conduction mechanism follows the simple two band model (STB) and exhibits similarity to that of polycrystalline turbostratic graphite. Our analysis can be also applied to other atomically thin 2D materials nanostructured networks and therefore to enable fundamental understanding of their characteristics in order to optimize the optoelectronic properties.

Acknowledgements

This project was financially supported by NSF (ECCS 1128335). CM acknowledges the award of a Royal Society University Research Fellowship by the UK Royal Society.

References

1 S. Stankovich, D. A. Dikin, G. H. B. Dommett, K. M. Kohlhaas, E. J. Zimney, E. A. Stach, R. D. Piner, S. T. Nguyen and R. S. Ruoff, *Nature*, 2006, **442**, 282–286.
2 Y. Hernandez, V. Nicolosi, M. Lotya, F. M. Blighe, Z. Sun, S. De, I. T. McGovern, B. Holland, M. Byrne, Y. K. Gun'Ko, J. J. Boland, P. Niraj, G. Duesberg, S. Krishnamurthy, R. Goodhue, J. Hutchison, V. Scardaci, A. C. Ferrari and J. N. Coleman, *Nat. Nanotechnol.*, 2008, **3**, 563–568.
3 J. N. Coleman, M. Lotya, A. O'Neill, S. D. Bergin, P. J. King, U. Khan, K. Young, A. Gaucher, S. De, R. J. Smith, I. V. Shvets, S. K. Arora, G. Stanton, H.-Y. Kim, K. Lee, G. T. Kim, G. S. Duesberg, T. Hallam, J. J. Boland, J. J. Wang, J. F. Donegan, J. C. Grunlan, G. Moriarty, A. Shmeliov, R. J. Nicholls, J. M. Perkins, E. M. Grieveson, K. Theuwissen, D. W. McComb, P. D. Nellist and V. Nicolosi, *Science*, 2011, **331**, 568–571.
4 G. Eda, H. Yamaguchi, D. Voiry, T. Fujita, M. Chen and M. Chhowalla, *Nano Lett.*, 2011, **11**, 5111–5116.
5 E. B. Secor, P. L. Prabhumirashi, K. Puntambekar, M. L. Geier and M. C. Hersam, *J. Phys. Chem. Lett.*, 2013, **4**, 1347–1351.
6 F. Bonaccorso, Z. Sun, T. Hasan and A. C. Ferrari, *Nat. Photonics*, 2010, **4**, 611–622.
7 T. Ramanathan, A. A. Abdala, S. Stankovich, D. A. Dikin, A. M. Herrera, R. D. Piner, D. H. Adamson, H. C. Schniepp, X. Chen, R. S. Ruoff, S. T. Nguyen, I. A. Aksay, R. K. Prud'Homme and L. C. Brinson, *Nat. Nanotechnol.*, 2008, **3**, 327–331.
8 G. Eda, H. E. Unalan, N. Rupesinghe, G. A. J. Amaratunga and M. Chhowalla, *Appl. Phys. Lett.*, 2008, **93**, 233502–233503.
9 Y. T. Liang, B. K. Vijayan, K. A. Gray and M. C. Hersam, *Nano Lett.*, 2011, **11**, 2865–2870.
10 S. Yang, X. Feng and K. Müllen, *Adv. Mater.*, 2011, **23**, 3575–3579.
11 S. C. De and N. Jonathan, *MRS Bull.*, 2011, **36**, 774–781.
12 G. Eda, C. Mattevi, H. Yamaguchi, H. Kim and M. Chhowalla, *J. Phys. Chem. C*, 2009, **113**, 15768–15771.
13 Q. Cao and J. A. Rogers, *Adv. Mater.*, 2009, **21**, 29–53.
14 J.-H. Ahn, H.-S. Kim, K. J. Lee, S. Jeon, S. J. Kang, Y. Sun, R. G. Nuzzo and J. A. Rogers, *Science*, 2006, **314**, 1754–1757.
15 J. Malig, J. M. Englert, A. Hirsch and D. M. Guldi, *Electrochem. Soc. Interface*, 2011, **20**, 53.

16 F. Torrisi, T. Hasan, W. Wu, Z. Sun, A. Lombardo, T. S. Kulmala, G.-W. Hsieh, S. Jung, F. Bonaccorso, P. J. Paul, D. Chu and A. C. Ferrari, *ACS Nano*, 2012, **6**, 2992–3006.
17 K. S. Novoselov, V. I. Falko, L. Colombo, P. R. Gellert, M. G. Schwab and K. Kim, *Nature*, 2012, **490**, 192–200.
18 G. Eda, G. Fanchini and M. Chhowalla, *Nat. Nanotechnol.*, 2008, **3**, 270–274.
19 D. A. Dikin, S. Stankovich, E. J. Zimney, R. D. Piner, G. H. B. Dommett, G. Evmenenko, S. T. Nguyen and R. S. Ruoff, *Nature*, 2007, **448**, 457–460.
20 H. Yamaguchi, G. Eda, C. Mattevi, H. Kim and M. Chhowalla, *ACS Nano*, 2010, **4**, 524–528.
21 A. Liscio, G. P. Veronese, E. Treossi, F. Suriano, F. Rossella, V. Bellani, R. Rizzoli, P. Samori and V. Palermo, *J. Mater. Chem.*, 2011, **21**, 2924–2931.
22 X. Liu, E. F. McCandlish, L. E. McCandlish, K. Mikulka-Bolen, R. Ramesh, F. Cosandey, G. A. Rosse tti and R. E. Riman, *Langmuir*, 2005, **21**, 3207–3212.
23 R. E. Riman and L. E. McCandlish, *US. Pat.*, 7, 022, 303, 2006
24 I. Langmuir and V. J. Schaefer, *J. Am. Chem. Soc.*, 1938, **60**, 1351–1360.
25 U. Khan, H. Porwal, A. O'Neill, K. Nawaz, P. May and J. N. Coleman, *Langmuir*, 2011, **27**, 9077–9082.
26 S. Barwich, U. Khan and J. N. Coleman, *J. Phys. Chem. C*, 2013, **117**, 19212–19218.
27 M. M. Cross, *Rheol. Acta*, 1979, **18**, 609–614.
28 G. Marrucci and P. L. Maffettone, *Macromolecules*, 1989, **22**, 4076–4082.
29 P. Werner, R. Verdejo, F. Wöllecke, V. Altstädt, J. K. W. Sandler and M. S. P. Shaffer, *Adv. Mater.*, 2005, **17**, 2864–2869.
30 U. Khan, A. O'Neill, M. Lotya, S. De and J. N. Coleman, *Small*, 2010, **6**, 864–871.
31 C. M. White, P. C. Rohar, G. A. Veloski and R. R. Anderson, *Energy Fuels*, 1997, **11**, 1105–1106.
32 C. s. Berrueco, P. A. l. S. Venditti, T. J. Morgan, A. A. Herod, M. Millan and R. Kandiyoti, *Energy Fuels*, 2009, **23**, 3008–3015.
33 A. C. Ferrari, J. C. Meyer, V. Scardaci, C. Casiraghi, M. Lazzeri, F. Mauri, S. Piscanec, D. Jiang, K. S. Novoselov, S. Roth and A. K. Geim, *Phys. Rev. Lett.*, 2006, **97**, 187401.
34 S. Stankovich, D. A. Dikin, R. D. Piner, K. A. Kohlhaas, A. Kleinhammes, Y. Jia, Y. Wu, S. T. Nguyen and R. S. Ruoff, *Carbon*, 2007, **45**, 1558–1565.
35 A. Eckmann, A. Felten, A. Mishchenko, L. Britnell, R. Krupke, K. S. Novoselov and C. Casiraghi, *Nano Lett.*, 2012, **12**, 3925–3930.
36 J. N. Coleman, *Acc. Chem. Res.*, 2012, **46**, 14–22.
37 C. Mattevi, G. Eda, S. Agnoli, S. Miller, K. A. Mkhoyan, O. Celik, D. Mastrogiovanni, G. Granozzi, E. Garfunkel and M. Chhowalla, *Adv. Funct. Mater.*, 2009, **19**, 2577–2583.
38 D.-Q. Yang and E. Sacher, *Langmuir*, 2006, **22**, 860–862.
39 M. W. A. Kuijpers, P. D. Iedema, M. F. Kemmere and J. T. F. Keurentjes, *Polymer*, 2004, **45**, 6461–6467.
40 F. Hennrich, R. Krupke, K. Arnold, J. A. Rojas Stütz, S. Lebedkin, T. Koch, T. Schimmel and M. M. Kappes, *J. Phys. Chem. B*, 2007, **111**, 1932–1937.
41 S. De, P. J. King, P. E. Lyons, U. Khan and J. N. Coleman, *ACS Nano*, 2010, **4**, 7064–7072.
42 L. J. Cote, F. Kim and J. Huang, *J. Am. Chem. Soc.*, 2008, **131**, 1043–1049.
43 X. Li, G. Zhang, X. Bai, X. Sun, X. Wang, E. Wang and H. Dai, *Nat. Nanotechnol.*, 2008, **3**, 538–542.
44 Z. Tang, J. Zhuang and X. Wang, *Langmuir*, 2010, **26**, 9045–9049.
45 R. R. Nair, P. Blake, A. N. Grigorenko, K. S. Novoselov, T. J. Booth, T. Stauber, N. M. R. Peres and A. K. Geim, *Science*, 2008, **320**, 1308.
46 H. S. Skulason, P. E. Gaskell and T. Szkopek, *Nanotechnology*, 2010, **21**, 295709.
47 Q. Zheng, W. H. Ip, X. Lin, N. Yousefi, K. K. Yeung, Z. Li and J.-K. Kim, *ACS Nano*, 2011, **5**, 6039–6051.
48 M. Lotya, Y. Hernandez, P. J. King, R. J. Smith, V. Nicolosi, L. S. Karlsson, F. M. Blighe, S. De, Z. Wang, I. T. McGovern, G. S. Duesberg and J. N. Coleman, *J. Am. Chem. Soc.*, 2009, **131**, 3611–3620.
49 D. S. McLachlan, M. Blaszkiewicz and R. E. Newnham, *J. Am. Ceram. Soc.*, 1990, **73**, 2187–2203.
50 D. S. McLachlan, *J. Phys., Colloq.*, 1985, **18**, 1891.
51 A. Celzard, E. McRae, C. Deleuze, M. Dufort, G. Furdin and J. F. Marêché, *Phys. Rev. B: Condens. Matter*, 1996, **53**, 6209–6214.
52 S. Wei-Li, C. Mao-Sheng, L. Ming-Ming, Y. Jian, J. Hong-Fei, H. Zhi-Ling, L. Jia, Y. Jie and F. Li-Zhen, *Nanotechnology*, 2013, **24**, 115708.
53 B. Zhang, Y. Yu, Y. Liu, Z.-D. Huang, Y.-b. He and J.-K. Kim, *Nanoscale*, 2013, **5**, 2100–2106.
54 D. B. Gingold and C. J. Lobb, *Phys. Rev. B: Condens. Matter*, 1990, **42**, 8220–8224.
55 D. J. Frank and C. J. Lobb, *Phys. Rev. B*, 1988, **37**, 302–307.
56 A. Celzard, J. F. Marêché and G. Furdin, *Prog. Mater. Sci.*, 2005, **50**, 93–179.
57 Y. T. Liang and M. C. Hersam, *J. Am. Chem. Soc.*, 2010, **132**, 17661–17663.
58 S. Biswas and L. T. Drzal, *Nano Lett.*, 2008, **9**, 167–172.
59 J. H. Lee, D. W. Shin, V. G. Makotchenko, A. S. Nazarov, V. E. Fedorov, J. H. Yoo, S. M. Yu, J.-Y. Choi, J. M. Kim and J.-B. Yoo, *Small*, 2010, **6**, 58–62.
60 A. A. Green and M. C. Hersam, *Nano Lett.*, 2009, **9**, 4031–4036.
61 S. De, P. J. King, M. Lotya, A. O'Neill, E. M. Doherty, Y. Hernandez, G. S. Duesberg and J. N. Coleman, *Small*, 2010, **6**, 458–464.
62 P. Blake, P. D. Brimicombe, R. R. Nair, T. J. Booth, D. Jiang, F. Schedin, L. A. Ponomarenko, S. V. Morozov, H. F. Gleeson, E. W. Hill, A. K. Geim and K. S. Novoselov, *Nano Lett.*, 2008, **8**, 1704–1708.
63 N. Behabtu, J. R. Lomeda, M. J. Green, A. L. Higginbotham, A. Sinitskii, D. V. Kosynkin, D. Tsentalovich, A. N. G. Parra-Vasquez, J. Schmidt, E. Kesselman, Y. Cohen, Y. Talmon, J. M. Tour and M. Pasquali, *Nat. Nanotechnol.*, 2010, **5**, 406–411.
64 C. A. Klein, *Rev. Mod. Phys.*, 1962, **34**, 56–79.
65 S. De and J. N. Coleman, *ACS Nano*, 2010, **4**, 2713–2720.

66 X. Liang, Z. Fu and S. Y. Chou, *Nano Lett.*, 2007, **7**, 3840–3844.
67 N. F. Mott, *Philos. Mag.*, 1969, **19**, 835–852.
68 P. Sheng, E. K. Sichel and J. I. Gittleman, *Phys. Rev. Lett.*, 1978, **40**, 1197–1200.
69 C. A. Neugebauer and M. B. Webb, *J. Appl. Phys.*, 1962, **33**, 74–82.
70 T. Ishiguro, H. Kaneko, Y. Nogami, H. Ishimoto, H. Nishiyama, J. Tsukamoto, A. Takahashi, M. Yamaura, T. Hagiwara and K. Sato, *Phys. Rev. Lett.*, 1992, **69**, 660–663.
71 M. Reghu, Y. Cao, D. Moses and A. J. Heeger, *Phys. Rev. B: Condens. Matter*, 1993, **47**, 1758–1764.
72 A. M. Nardes, M. Kemerink, R. A. J. Janssen, J. A. M. Bastiaansen, N. M. M. Kiggen, B. M. W. Langeveld, A. J. J. M. van Breemen and M. M. de Kok, *Adv. Mater.*, 2007, **19**, 1196–1200.
73 A. B. Kaiser, C. Gómez-Navarro, R. S. Sundaram, M. Burghard and K. Kern, *Nano Lett.*, 2009, **9**, 1787–1792.
74 S. Ravi, A. B. Kaiser and C. W. Bumby, *Chem. Phys. Lett.*, 2010, **496**, 80–85.
75 A. Behnam, A. Biswas, G. Bosman and A. Ural, *Phys. Rev. B: Condens. Matter Mater. Phys.*, 2010, **81**, 125407.
76 K. Yanagi, H. Udoguchi, S. Sagitani, Y. Oshima, T. Takenobu, H. Kataura, T. Ishida, K. Matsuda and Y. Maniwa, *ACS Nano*, 2010, **4**, 4027–4032.
77 T. M. Barnes, J. L. Blackburn, J. van de Lagemaat, T. J. Coutts and M. J. Heben, *ACS Nano*, 2008, **2**, 1968–1976.
78 Z. Li, H. R. Kandel, E. Dervishi, V. Saini, Y. Xu, A. R. Biris, D. Lupu, G. J. Salamo and A. S. Biris, *Langmuir*, 2008, **24**, 2655–2662.
79 V. Pantin, J. Avila, M. A. Valbuena, P. Esquinazi, M. E. Dávila and M. C. Asensio, *J. Phys. Chem. Solids*, 2006, **67**, 546–551.
80 D. W. McKee, *Annu. Rev. Mater. Sci.*, 1973, **3**, 195–231.
81 C. A. Klein, *J. Appl. Phys.*, 1964, **35**, 2947–2957.
82 Y. Zhang, J. P. Small, W. V. Pontius and P. Kim, *Appl. Phys. Lett.*, 2005, **86**, 073104–073103.
83 M. F. Craciun, S. Russo, M. Yamamoto, J. B. Oostinga, A. F. Morpurgo and S. Tarucha, *Nat. Nanotechnol.*, 2009, **4**, 383–388.
84 L. D. Woolf, J. Chin, Y. R. Lin-Liu and H. Ikezi, *Phys. Rev. B*, 1984, **30**, 861–869.